Volumetric flattening: an interpretation tool

Jesse Lomask* **and Antoine Guitton‡**

**Stanford Exploration Project, Mitchell Bldg., Department of Geophysics,*

Stanford University, Stanford, CA 94305-2215

‡*3DGeo Development Inc.*

Santa Clara, CA 95054

(October 26, 2006)

Volumetric flattening is a method for automatically flattening entire 3D seismic cubes without manual picking. This is an efficient algorithm that intrinsically performs automatic dense picking on entire 3D cubes at once. The method involves first calculating local dips (step-outs) everywhere in the data using a dip estimation technique. These dips are resolved into time shifts (or depth shifts) via a non-linear least-squares problem. The data are subsequently vertically shifted according to the summed time shifts to output a flattened volume.

A most attractive feature of the previously described flattening technique is that it requires no manual picking. This would be fine if all data sets had reasonably accurate estimated dips, but in the real world automatic flattening can produce results that are not perfect. Noise, both coherent and otherwise, can overwhelm the dip estimation causing reflectors in those areas to not be flat. Multiples, for example, are significant source of coherent noise that can contaminate the dip field. Although certain faults with tip-lines (terminations) encased within the data cube can be flattened if a fault model is provided, faults that cut across the entire data cube cannot. Consequently, it would be useful to have the ability to add some geological constraints to restrict the flattening result in areas of poor data quality while allowing it to efficiently tackle other areas where estimated dips are more

accurate. Additionally, correlations can be used as constraints to reconstruct across faults that do not terminate within the data cube.

Here we demonstrate several interpretive applications of volumetric flattening with and without constraints. This robust and efficient algorithm provides interpretation solutions that honor more, if not all, of the available data. Bienati and Spagnolini (2001) originally presented a least-squares approach to numerically resolve the dips into time shifts for the purpose of auto-picking individual horizons and flattening gathers. The first volumetric flattening results, where entire volumes are flattened to create volumes of horizon slices, were introduced to the seismic industry by Lomask and Claerbout (2002). Subsequently, Lomask (2003) and Lomask et al. (2006) developed volumetric flattening further.

Methodology

Ordinarily, in order to flatten a single surface, each sample is shifted vertically to match a chosen reference point. For instance, this reference point can be the intersection of the horizon and a well pick. For multiple horizons, this reference point becomes a vertical line (reference trace). In Figure 1 is a cartoon of a horizon and the mapping field represented by arrows. In order to flatten 3D cubes, the objective is to find a mapping field $\boldsymbol{\tau}(x, y, t)$ such that each time slice of this field contains the locations of all the data points along the horizon that happens to intersect the reference trace at that time slice. This $\boldsymbol{\tau}$ field is found by fitting surfaces, in a least-squares sense, to local dips. The dips can be efficiently calculated using a local plane-wave destructor filter as described by Claerbout (1992) or with an improved dip estimator that is described by Fomel (2002). We primarily use the latter. For each point in the data cube, two components of dip are estimated in the x and y directions.

Therefore, volumetric flattening is essentially a two-steps process where dips in x and y directions

are estimated, and where $\boldsymbol{\tau}(x,y,t)$ is computed by integrating the dips in the two directions (Lomask, 2006). For noisy data, or for faults cutting across the whole volume, we incorporate weights and masks. The weights help minimizing the influence of bad dips whereas the masks help constraining known shift values. Both effects are illustrated in the next section.

UNCONSTRAINED RESULTS

Here, we demonstrate this flattening method's efficacy on synthetic and field 3D data sets. We start with simple unconstrained flattening results and then illustrate how this method can handle data with faults and folds on several 3D field data sets with varying degrees of structural complexity with a minimal amount of constraints.

Gulf of Mexico salt piercement data

Figure 2 is a field 3D data cube from the Gulf of Mexico provided by Chevron. It consists of structurally simple horizons that have been warped up around a salt piercement. Several channels can be seen in the time slice at the top of Figure 2 but are largely obscured by the gradual amplitude overprint of a nearly flat horizon that is cut by the time slice. Also, hints of several channels can be seen near the salt piercement. Figure 3 shows the flattened output of the data in Figure 2. We flattened this data set using the method without weights. The seismic cube has been converted from a stack of time slices to a stack of horizon slices. The entire datacube ($34 \times 450 \times 450$ samples) was flattened in about two minutes on a single Intel Xeon 2.40 GHZ processor and required minimal parameter adjustment (only smoothing of the dips). Notice that the gradual amplitude overprint present in the unflattened data is no longer present in the flattened data. This is because horizons are no longer cutting across the image. Several channels are now easily visible on the horizon slice. Also, the beds

adjacent to the salt dome have been partially reconstructed causing the salt to occupy a smaller area in Figure 3. Additionally, a channel (within oval) can be seen adjacent to the salt.

The $\boldsymbol{\tau}$ field used to flatten the data has been roughened with the helix derivative (Claerbout, 1999) and is displayed in Figure 4. The Helix derivative is estimated after spectral factorization of the Laplacian operator into a minimum phase filter. As such, the helix derivative behaves similarly to a gradient operator while being more isotropic. Notice that the channels are clearly visible. This means that the subtle dip changes from the channel boundaries were picked up by the dip estimation and subsequently used for flattening. This implies that the flattening result in Figure 3 could possibly reveal more channel information by first applying a low pass filter or smoothing to the input dips. In this way, the flattening algorithm will preserve channel boundaries. Alternatively, the helix derivative of the $\boldsymbol{\tau}$ field as a channel map can be improved by less smoothing of the dips. The striations present in the vertical sections could be eliminated by using more regularization.

Figure 5 displays three horizons overlain on the original data in Figure 2. The horizons track the reflectors on the flanks of the salt well. Within the salt, the horizons gradually diverge from their respective reflector events as the estimated dip becomes less accurate. The time slice at the top displays the swath of a tracked horizon.

North Sea unconformity data

Figure 6 shows a 3D North Sea data set. Marked by considerable folding and a sharp angular unconformity, this data presents a real-world flattening challenge. The result of flattening is displayed in Figure 8. A stretch mute has been applied to highlight areas of no deposition. This is something like a Wheeler diagram (Wheeler, 1958). The result displaying a few of the automatically picked horizons is shown in Figure 7. Bear in mind that although every horizon was picked by this method, we are

only displaying a small subset. The time slice at the top shows the swaths of a few horizons. Overall, the tracked horizons track up to and along the unconformity, although some errors occur where the data quality is poor and, as a result, the estimated dips are inaccurate.

Besides using the stretching of the data, another way highlight the unconformity (or pinchouts in general) in Figure 6, we can apply the inverse of flattening (unflattening) to a volume filled with 1s. Where multiple 1s are mapped to the same location, we will add them. The resulting volume is displayed in Figure 9. This is a cube highlighting areas where horizons are overlaying one another. In other words, it is highlighting pinchouts. The brightest pinchout is associated with the major angular unconformity near 2000 m depth. It should be pointed out that the results are sensitive to the location of the reference trace. If the reference trace is placed in the thickest section then it will highlight the pinchouts. If the reference trace is in the thinnest location, then it will not successfully identify the pinchouts.

CONSTRAINED RESULTS

We conducted tests of the constrained flattening method on two 3D data sets from the Gulf of Mexico and the North Sea. The first example illustrates how a single pair of traces can be manually correlated and passed to the constrained flattening method to reconstruct across faults. The second example illustrates how a few individual horizon picks can improve the overall flattening result. For both examples, shift values are first estimated independently of the volumetric flattening method. These values are then passed to the inversion and held constant during the iterations thanks to a masking operator.

Gulf of Mexico faulted data

In Figure 10 is a 3D Gulf of Mexico data set provided by Chevron. The manually interpreted fault model is displayed in Figure 11. Two faults are identified in the figure. Fault 1 has part of its tip-line encased within the cube as can be observed by its termination in the time slice. Fault 2, on the other hand, does not terminate within the data cube. Because Fault 1 terminates within the data cube, no constraints need to be provided to flatten across it, however, Fault 2 requires some picking. In this case, we picked one vertical pair of traces across Fault 2. Then we applied a weighted flattening method with the weights being the picked fault model. We also used a binary mask which takes the value of one for unconstrained model locations and zero for constrained model locations. The weights will ignore dip measurements at the fault locations, which prevents the volumetric flattening from picking the wrong reflectors across the fault plane. The mask guarantees that the a-priori shift values at the individually picked horizons won't change during the inversion.

Figure 12 is flattened volume of the data in Figure 10. Notice the horizons are reconstructed across both faults. Notice the faint outline of a channel that is annotated on the figure. Another view of the same cube is displayed in Figure 13. Several stratigraphic features are reconstructed across both faults. In addition to a fault model, the only picks required were from a single trace of correlations across Fault 2. Also, the $\boldsymbol{\tau}$ field used to flatten this data is displayed in Figure 15.

In Figure 14 every 25th tracked horizon of the constrained flattening method in displayed. Notice the overlain horizons track their respective events across both faults. In short, we reconstructed this 3D volume by correlating a single pair of traces across a fault. It should be pointed out that an automatic fault indicator could substitute for the fault model, reducing the amount of manual interpretation even further.

A flattened cube with faults that is properly reconstructed implies that the slip distribution along

the fault surfaces have been captured within the $\boldsymbol{\tau}$ field. Factors governing the slip distribution include the stress field, proximity to other faults, rock strength, tectonic history, and loading rates (Pollard, 2001). If the slip distribution were easily and quickly obtained, it could be added to interpretation and processing work-flows.

In Figure 15 is the $\boldsymbol{\tau}$ field used to flatten the data in Figure 10. Notice that it changes in magnitude abruptly across the major fault, referred to as Fault 2. This is because the beds are shifted significantly from each other across the fault. The minor fault, Fault 1, can also be seen in this cube as well. Recall that this cube was flattened with a fault model and only one correlated pair of traces across Fault 2. Nothing more than a fault model was required to flatten across Fault 1. we extracted the $\boldsymbol{\tau}$ field values from either side of Fault 1 and differenced them. The contoured difference is shown in Figure 16. The contours show the vertical slip in time across the minor fault, Fault 1.

North Sea salt data

In Figure 17 is a 3D North Sea data set provided by Total. This data set has several issure including coherent noise and weak signal (see annotations). The flattening result is displayed in Figure 18. Several horizons that result from unconstrained flattening are displayed in Figure 19. Without constraints, each horizon is flattened independently. Although we are only displaying five horizons, we have actually tracked all of the horizons in the cube. This is a key feature of flattening. Whereas the top two of the displayed horizons are well tracked, the lowest three are not. Figure 20 displays the τ field that results from the unconstrained flattening. Notice that at approximately 1200 m depth there is a significant shift in the τ field. This marks where the salt boundary crosses the reference trace. The reference trace is located at the intersections of the panels at x=5040 m and y=3540 m. The salt interface is separating two regions of different dip and as a result is an angular unconformity. The τ

field is sensitive to the location of this boundary.

To introduce constraints to this data, we selected the bright salt reflector that is very close to the fourth picked horizon in Figure 19. Since the fourth horizon is close to the bright salt reflector, it would have made an acceptable constraint but we decided to improve its tracking result by adding twenty two manually interpreted points along the bright reflector. These twenty two points are displayed in Figure 21 as black dots. To use these twenty two points as constraints for the entire cube required two passes of the flattening algorithm. In the first pass, these individual points were passed to the flattening algorithm as constraints but only for that individual horizon. The resulting surface is also displayed in Figure 21.

The well tracked areas from the unconstrained result in 18 can easily be combined with the manually picked horizon to give an overall improved flattening solution. We merely pass both the top part of the unconstrained results and the manually picked surface as constraints. The result of this is displayed in Figure 22. Notice that now all of the horizons are well flattened. The picking result displayed in Figure 23 reveals that the first four reflectors displayed are accurately tracked. This result honors both the constraints and the dip data. To improve the fifth reflector, we would likely need more manual constraints.

ADDITIONAL FLATTENING APPLICATIONS

The flattening process has numerous post-stack applications. The ability to convert a data cube from time (or depth) to a horizon cube has obvious and immediate interpretive uses by simply presenting the data in a more geologically meaningful way. Additionally, the mapping from unflat to flat ($\boldsymbol{\tau}$ field) contains all of the information of the shapes of all of the reflectors in the data cube. This has potential ranging from isopach analysis to horizon shape attribute volumes. In the case of flattening with faults,

the flattening process automatically captures the slip distributions (fault contours) along the faults. This leads naturally to fault contour analysis which has numerous applications originally described in Lomask (2002). Lastly, knowledge of the combination of fault slip and horizon deformation can be related to local stress measurements.

The prestack applications of flattening are also numerous. The most obvious being gather alignment. Additionally, the $\boldsymbol{\tau}$ field can be used for tomographic velocity analysis (Guitton et al., 2004). Furthermore, the $\boldsymbol{\tau}$ field can be used to fit parametric curves from angle gathers for residual moveout velocity updating. Flattening can also be used to detect and quantify migration artifacts. Although still largely under-exploited in prestack applications, flattening has the ability to handle any number of dimensions.

Local stress volumes

Maerten et al. describe how flat simple models created with some basic knowledge about the regional stress field and rock properties can be deformed or forward modeled until agreement with the structure gleaned from seismic data is found. This involves deforming the layers and faults together. Once a match is achieved then they are able to create maps of the local stress field which can then be related to secondary fractures and faults caused by folding. Therefore, it seems like a straight forward application of flattening to incorporate the $\boldsymbol{\tau}$ field into an inversion process that creates local stress volumes.

Seismic processing

Similar to the local stress volumes, geologically meaningful models can be built by first creating a simple layered model (in 2 or 3D) and then unflattening it according to a Tau field. This Tau field

could come from a migrated image. Velocity or density models can be then created very easily.

Flattening can be also seen as a warping tool for migrated images. For instance, it is well known that PP and PS images from do not conform in depth. Both could be flattened, horizons could be aligned, and both results could be unflattened again, thus ensuring matching of the reflectors.

CONCLUSIONS AND DISCUSSION

We demonstrated that volumetric flattening with and without contraints can be used deliver useful full-volume interpretation solutions. This method efficiently and robustly flattens 3D seismic datasets. By using constraints, volumetric flattening finds solutions that combine the computer's ability to handle large multidimensional datasets with the human's strength in pattern recognition.

Data cubes with vertical, laterally limited faults can be flattened by applying a residual weight. This allows horizons to be tracked around the faults. The weight can be created from a previously determined fault model or coherence attribute. The weight merely identifies inaccurate dip values estimated at fault discontinuities so that they will be ignored within the inversion.

As demonstrated here, the ability to incorporate some picking allows the reconstruction of horizons across faults that cut across the entire data cube. An interpreter can pick a few points on a 2D line and then flatten the entire 3D cube. With computational improvements in both the algorithm and hardware, this method could be applied on the fly, as the interpreter adds new picks.

Also, as pointed out in Lomask (2003), geological features can be interpreted on the flattened horizon sections then subsequently unflattened into their original structural shape to tie with wells and other data.

The ability to use flattening in an iterative scheme is still under-exploited. Once a data cube

has been flattened, dips can be re-estimated on the flattened cube and then flattened again using the statistics of the dip as a measure of flatness. It seems plausible that this approach has the potential to greatly improve the quality of the flattening process. Furthermore, better flattening results can be obtained by first flattening low-passed versions of the data and gradually adding in higher frequencies.

The obtained estimate of $\boldsymbol{\tau}(x, y, t)$ has many potential uses; e.g., the proposed method can easily be adapted to flatten data cubes on one or any particular combination of horizons. This would assist geologists in analyzing thicknesses for rates of deposition and timing of structural events in growth faults. Furthermore, for faulted data sets that have been successfully reconstructed by this flattening method, the integrated time shifts contain the slip distributions along the fault planes.

SUGGESTED READING

The software used to generate the results in the paper is freely available in SEPLIB at http://sepwww.stanford.edu/software/seplib/.

ACKNOWLEDGMENT

We would like to thank Chevron and Total for supplying the data and their permission to publish the results. We would also like to acknowledge the financial support of the sponsors of the Stanford Exploration Project.

REFERENCES

Bienati, N. and U. Spagnolini, 2001, Multidimensional wavefront estimation from differential delays: IEEE Trans on Geoscience and Remote Sensing, **39**, no. 3, 655–664.

Claerbout, J. F., 1992, Earth Soundings Analysis: Processing Versus Inversion: Blackwell Scientific Publications.

Claerbout, J., 1999, Geophysical estimation by example: Environmental soundings image enhancement: Stanford Exploration Project, http://sepwww.stanford.edu/sep/prof/.

Fomel, S., 2002, Applications of plane-wave destruction filters: Geophysics, **67**, no. 6, 1946–1960.

Guitton, A., J. F. Claerbout, and J. M. Lomask, 2004, First order interval velocity estimates without picking: 74th SEG Meeting, Extended Abstracts, 2339–2342.

Lomask, J. and J. Claerbout, 2002, Flattening without picking: SEP–**112**, 141–150.

Lomask, J., A. Guitton, S. Fomel, and J. Claerbout, 2006, Flattening without picking: Geophysics, **71**, no. 4, 13–20.

Lomask, J., 2002, Fault contours from seismic: SEP–**111**, 295–309.

Lomask, J., 2003, Flattening 3D seismic cubes without picking: 73th SEG Meeting, Extended Abstracts, 1402–1405.

Lomask, J., 2006, Seismic volumetric flattening and segmentation: Ph.D. thesis, Stanford University.

Maerten, L., F. Maerten, and P. Gillespie, Poly3d: a 3d geomechanical program used to solve fault related problems in petroleum reservoirs: Hydrocarbon seal quantification: Stavanger, Norway, October 16-18 2000.

Pollard, D. Structural geology and geomechanics:. Internet, 2001. http://pangea.stanford.edu/geomech/Research/Research.htm.

Wheeler, H. E. ., 1958, Time stratigraphy: Bulletin of the american assocation of petroleum geologists, **42**, no. 5, 1047–1063.

LIST OF FIGURES

gether (pinchout) and is an indicator of unconformities.

10 Gulf of Mexico faulted data. The black lines superimposed onto the orthogonal sections identify the location of these sections: a time slice at time=1.584 s, an in-line section at y=3203 m, and a cross-line section at x=3116 m. The reference trace is located at x=2204 m and y=1259 m.

11 As Figure 10 displaying the manually picked fault model used for flattening.

12 As Figure 10 only after flattening. Notice that reflectors on both sides of both faults are properly reconstructed. Also, notice a sinusoidal channel that is annotated on the horizon slice.

13 As Figure 12 except displaying a different horizon slice, time=1.504 s. Several stratigraphic channel features are visible.

14 As Figure 10 only displaying every 25th tracked horizon of the constrained flattening method. The fault model (solid black) was manually picked.

15 As Figure 10 showing the $\boldsymbol{\tau}$ field used for flattening.

16 Fault contours from Fault 1 in Figure 10. The slip is measured in time. These were created by extracting and differencing the $\boldsymbol{\tau}$ field in Figure 15 from both sides of the fault.

17 North Sea salt data provided by Total. The black lines superimposed onto the orthogonal sections identify the location of these sections: a depth slice at time=1050 m, an in-line section at y=3540 m, and a cross-line section at x=5040 m. The reference trace is located at x=5040 m and y=3540 m, coincident with the intersection of the vertical sections.

18 As Figure 17 only after applying unconstrained flattening.

19 As Figure 17 except displaying five tracked horizons. Although we are only displaying five horizons, these flattening methods track all of the horizons in the data cube at once. This is an unconstrained solution. Notice that the third, fourth and fifth displayed horizons from the top are inaccurate.

20 As Figure 17 except displaying the τ field.

21 The 22 manually picked points and the auto-tracked surface flattening with the manually picked points as constraints. This surface corresponds to the bright salt boundary in Figure 17.

22 As Figure 17 only after flattening with constraints consisting of the manually influenced salt boundary and the upper portion of the unconstrained flattening result from Figure 18.

23 As Figure 17 except displaying five tracked horizons with constraints consisting of the manually influenced salt boundary and the upper portion of the unconstrained flattening result.

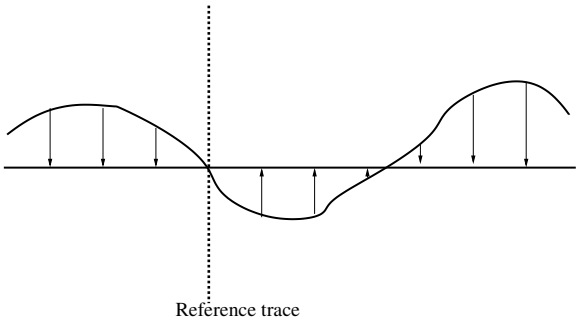

Figure 1.

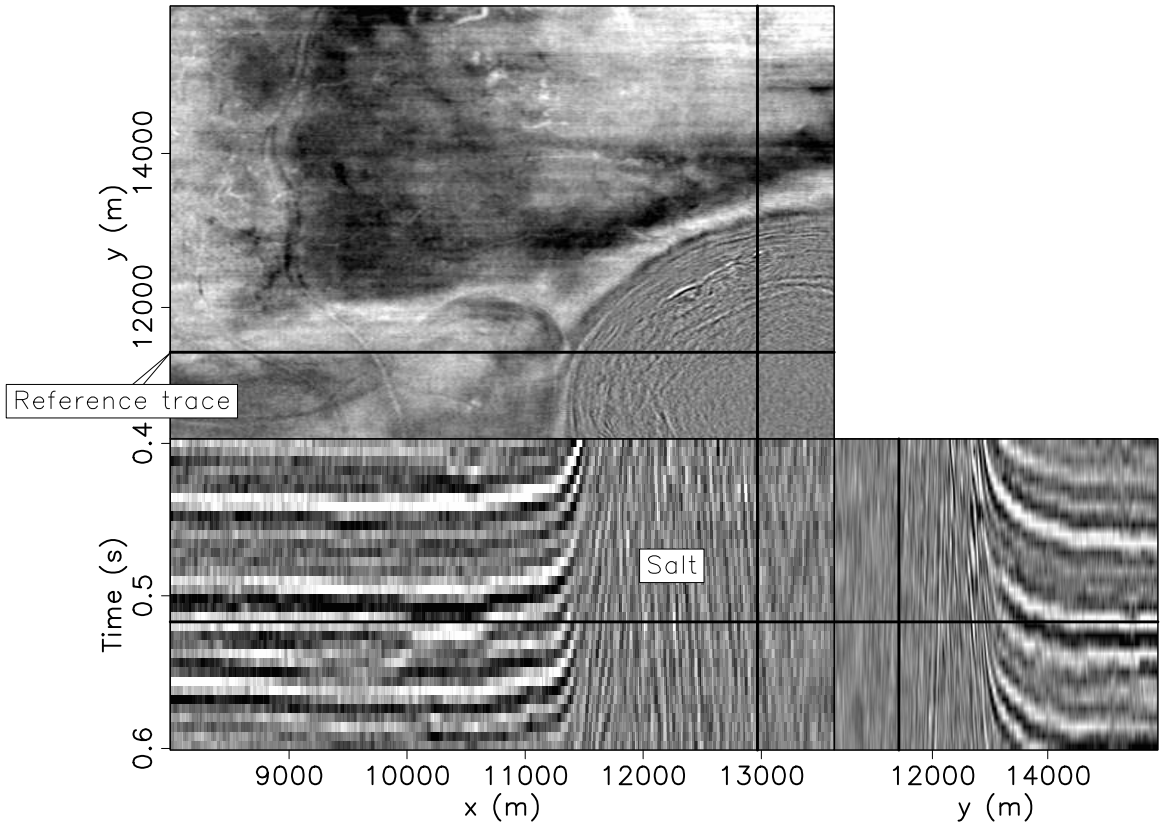
y (m)
14000
12000
Reference trace
0.4
Time (s)
0.5
0.6
Salt
9000
10000
11000
12000
13000
x (m)
12000
14000
y (m)

Figure 2.

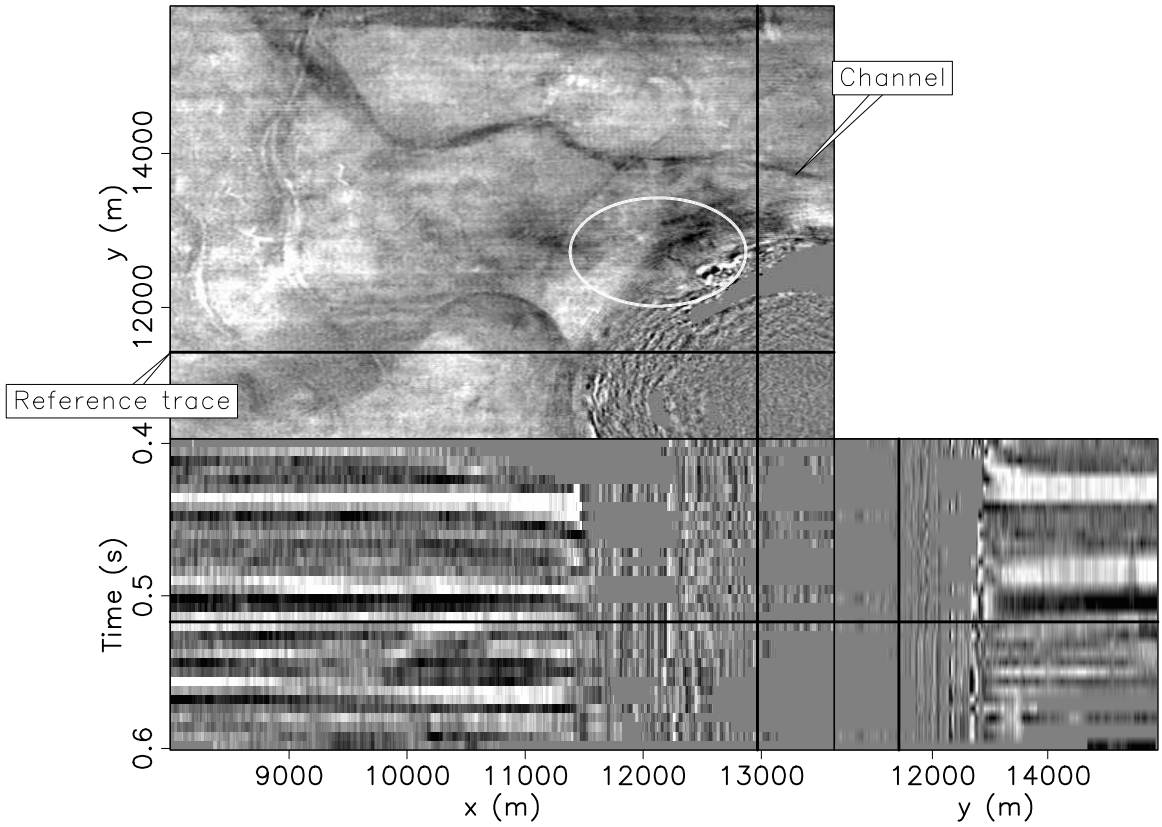
Channel
Reference trace
y (m)
14000
12000
Time (s)
0.4
0.5
0.6
9000
10000
11000
12000
13000
x (m)
12000
14000
y (m)

Figure 3.

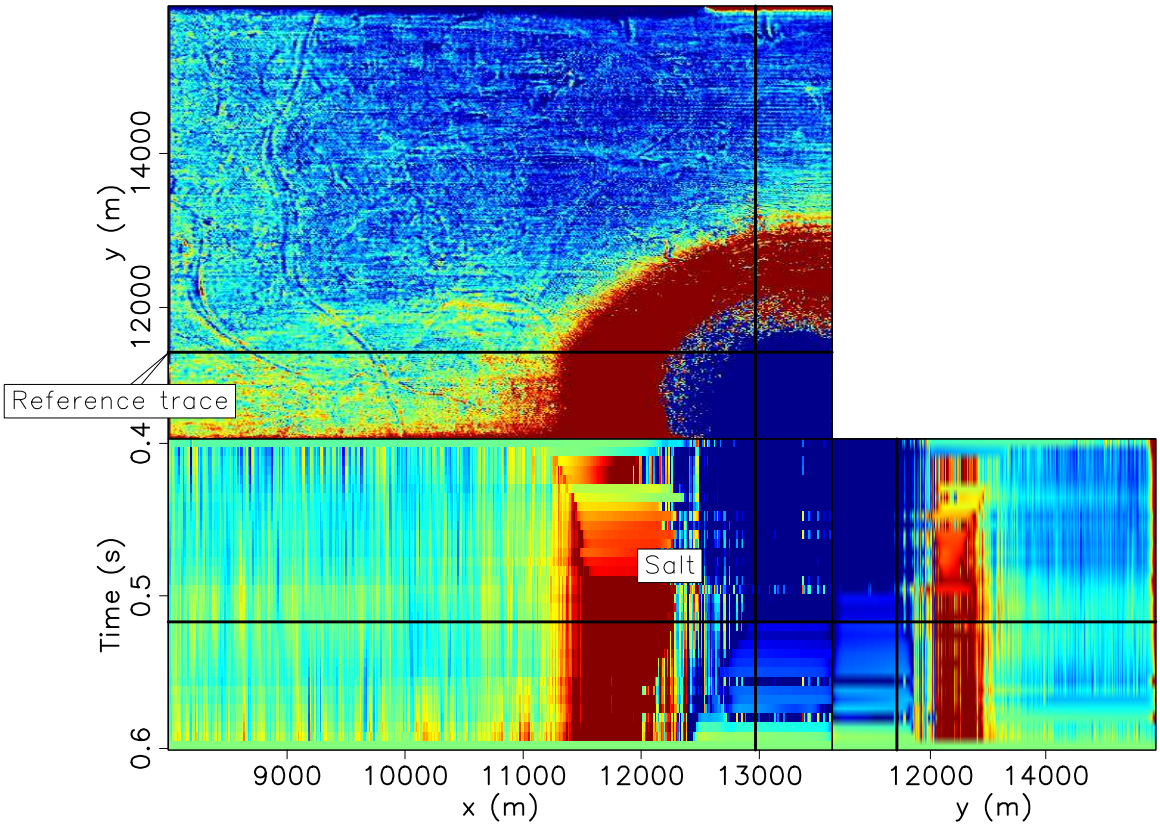
y (m)
14000
12000
Reference trace
0.4
Time (s)
0.5
0.6
Salt
9000
10000
11000
12000
13000
x (m)
12000
14000
y (m)

Figure 4.

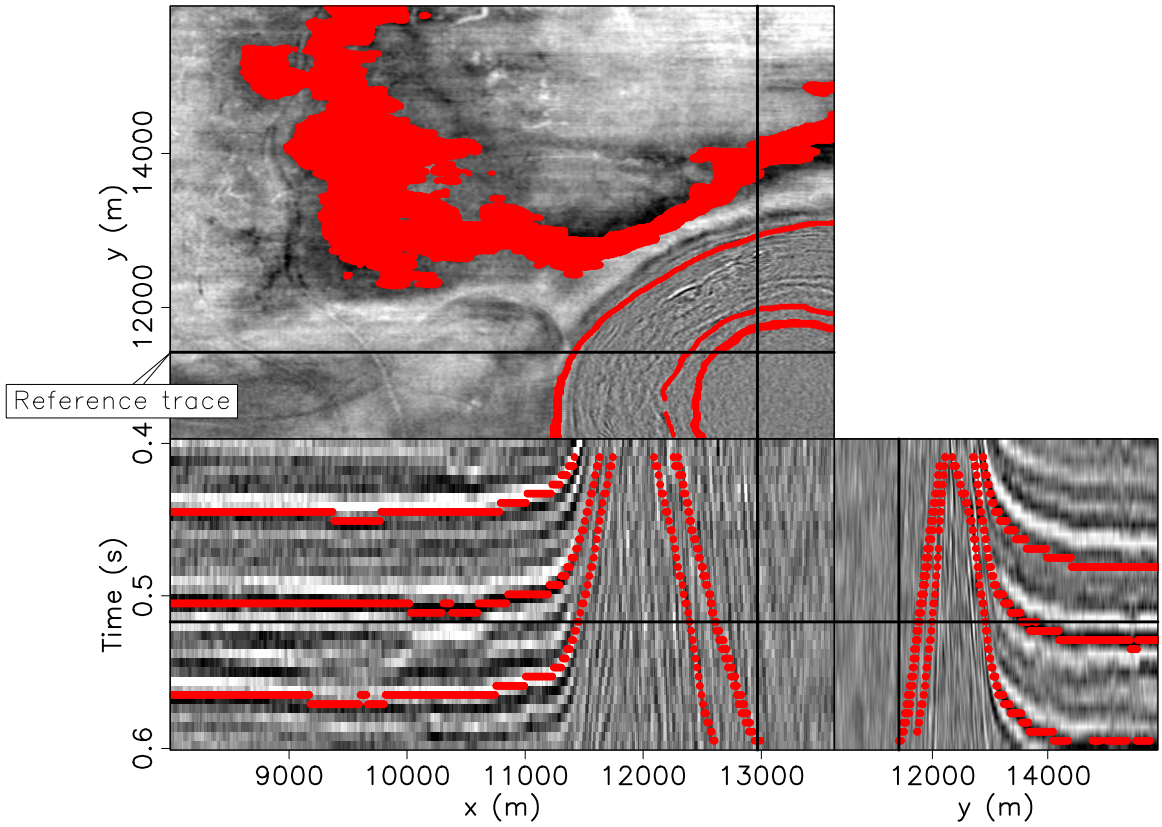
y (m)
12000
14000
Reference trace
Time (s)
0.4
0.5
0.6
9000
10000
11000
12000
13000
x (m)
12000
14000
y (m)

Figure 5.

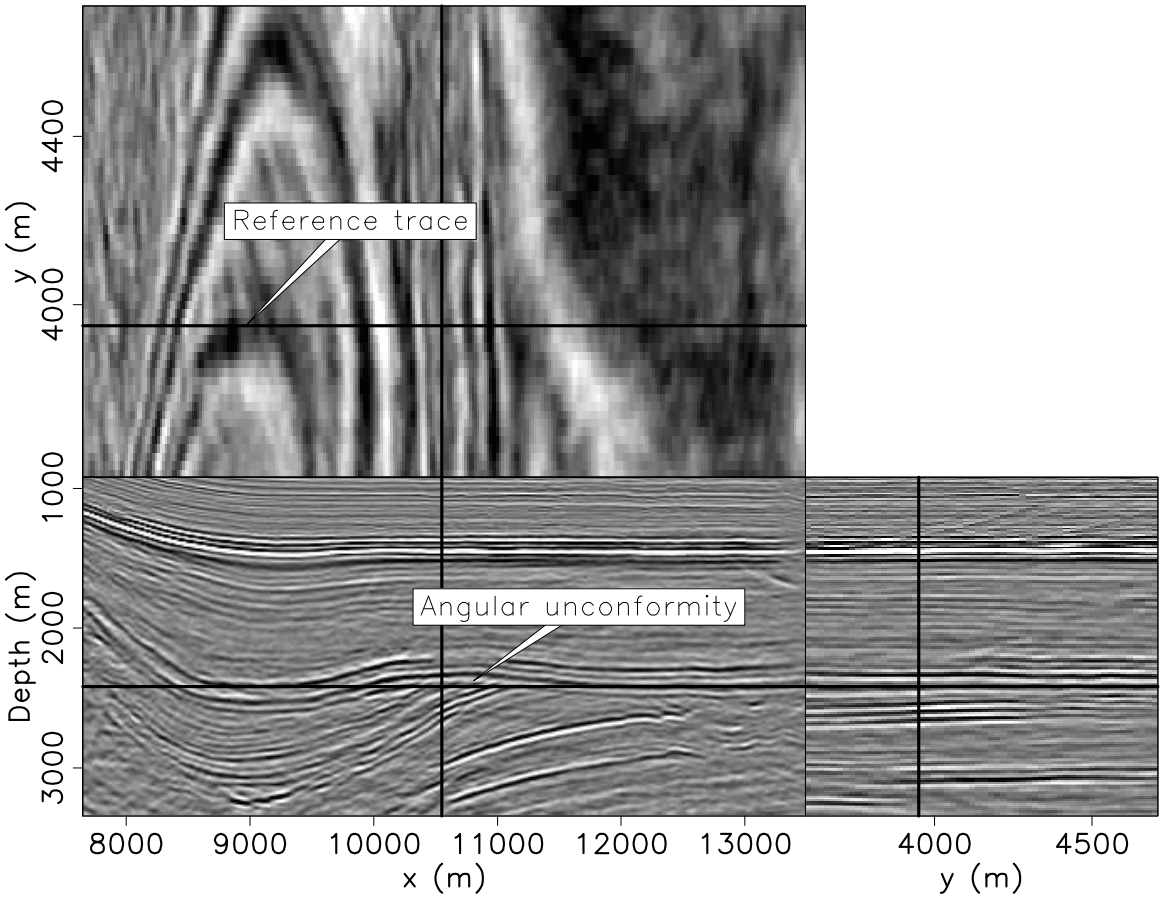
Reference trace
Angular unconformity
y (m)
4400
4000
1000
Depth (m)
2000
3000
8000
9000
10000
11000
12000
13000
x (m)
4000
4500
y (m)

Figure 6.

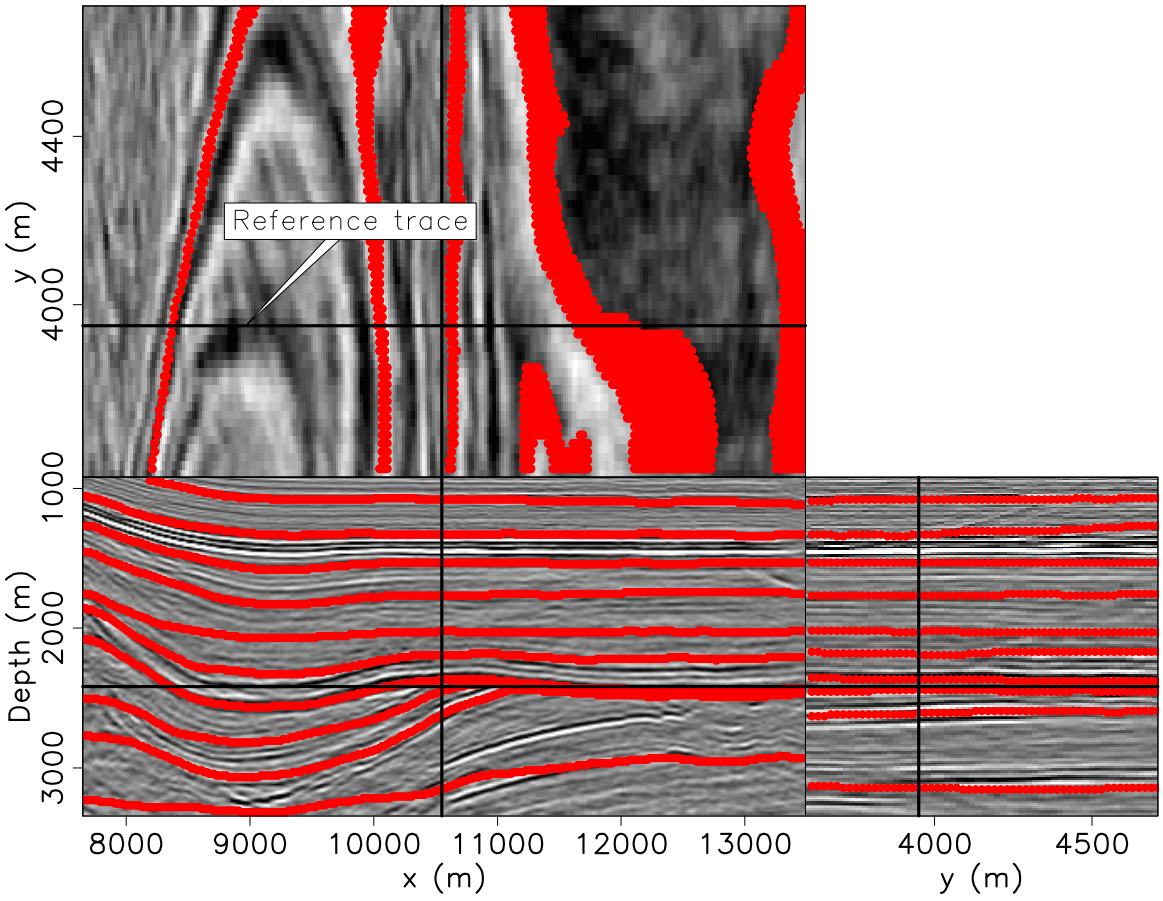
Reference trace
y (m)
4400
4000
1000
Depth (m)
2000
3000
8000
9000
10000
11000
12000
13000
x (m)
4000
4500
y (m)

Figure 7.

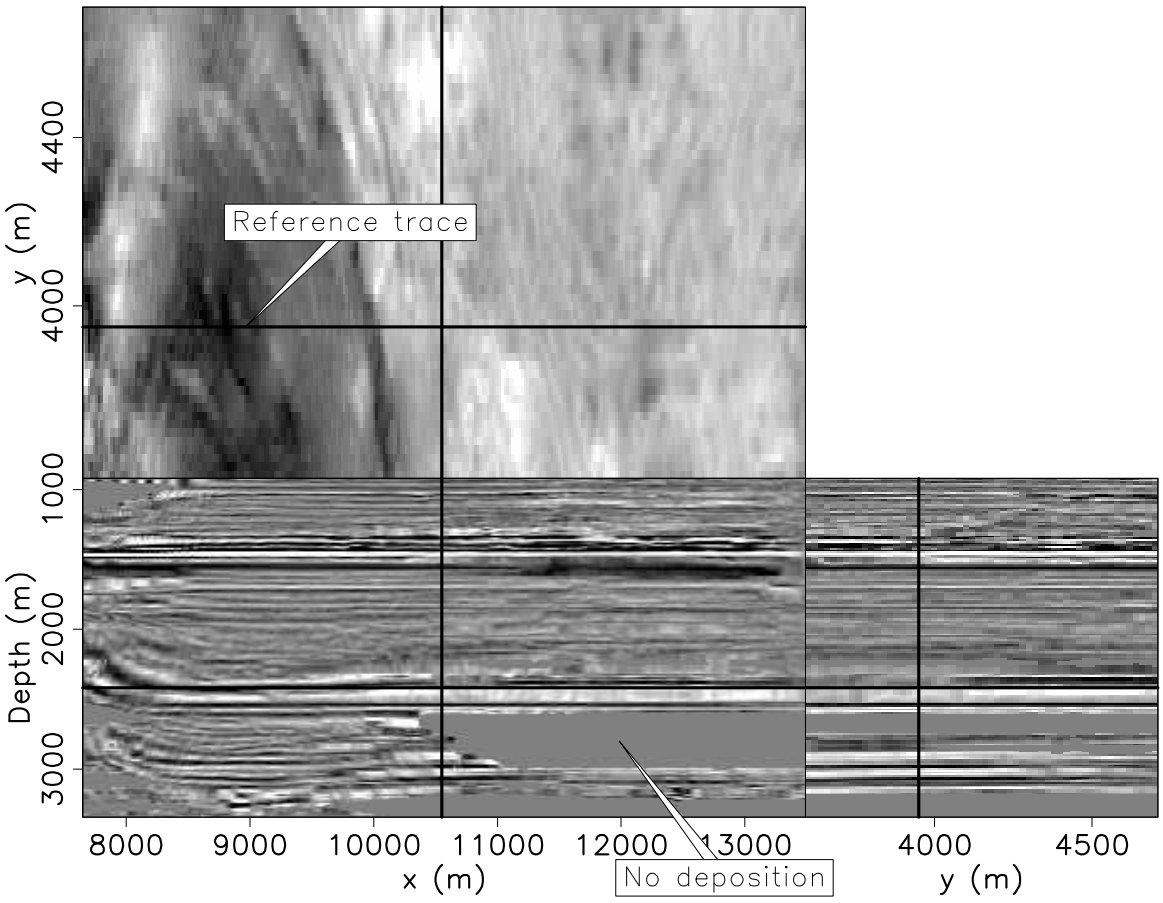
Reference trace
No deposition
y (m)
4400
4000
1000
Depth (m)
2000
3000
8000
9000
10000
11000
12000
13000
x (m)
4000
4500
y (m)

Figure 8.

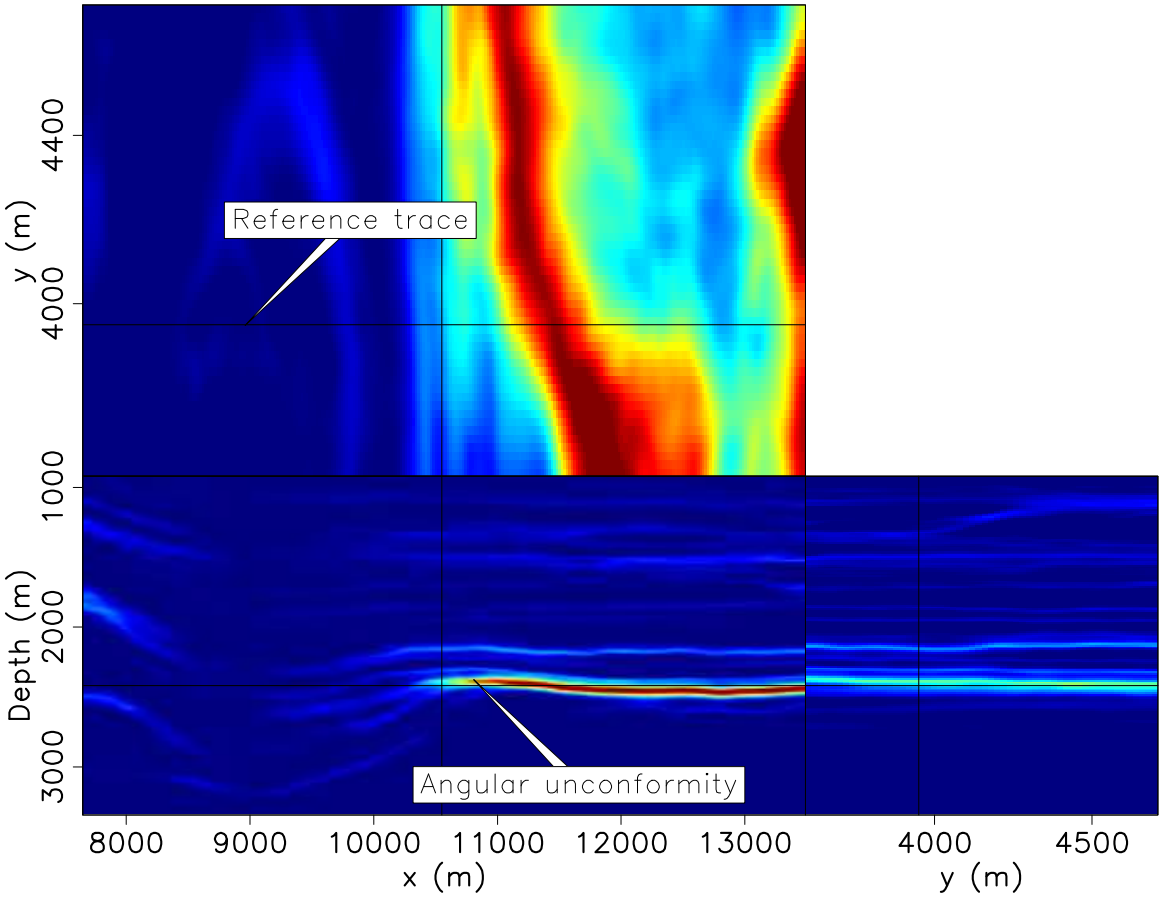
Reference trace
Angular unconformity
y (m)
4400
4000
1000
Depth (m)
2000
3000
8000
9000
10000
11000
12000
13000
x (m)
4000
4500
y (m)

Figure 9.

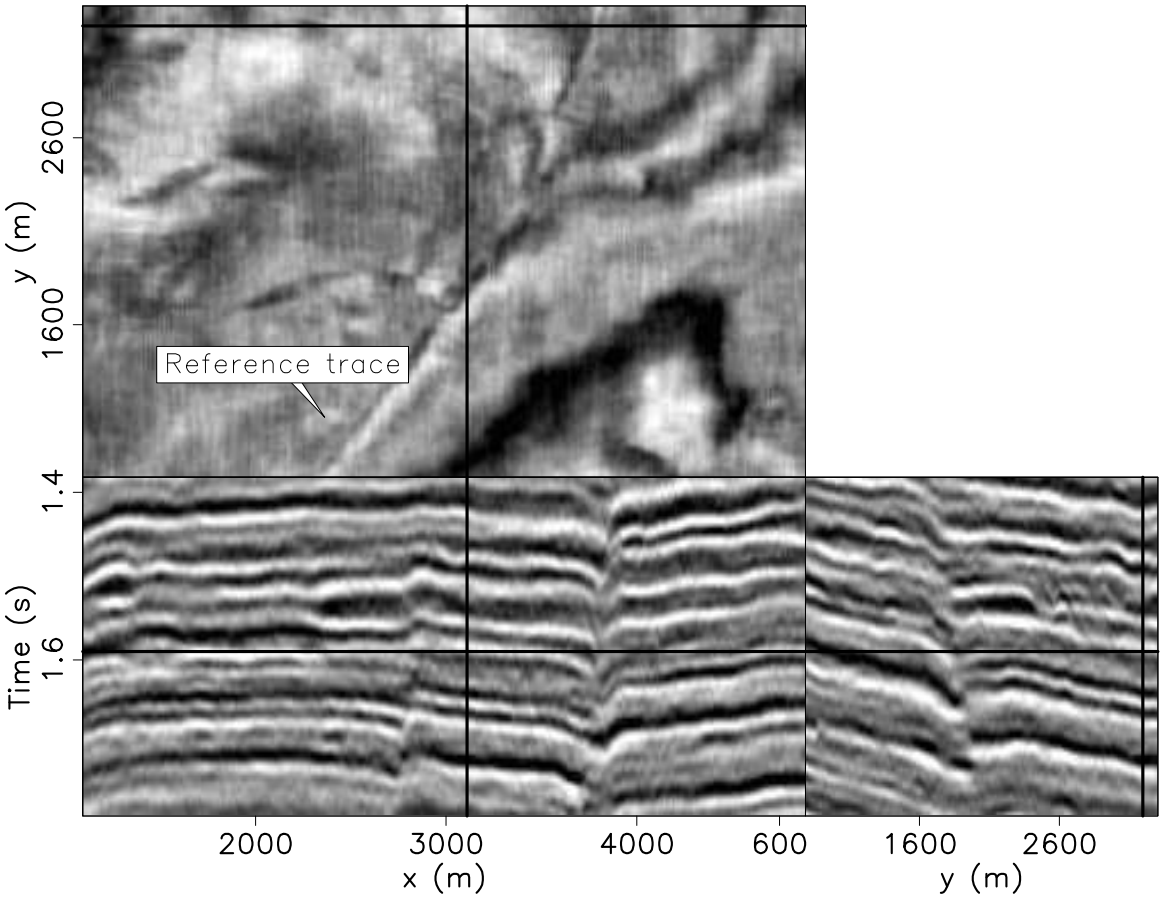
Reference trace
y (m)
2600
1600
Time (s)
1.4
1.6
2000
3000
x (m)
4000
600
1600
2600
y (m)

Figure 10.

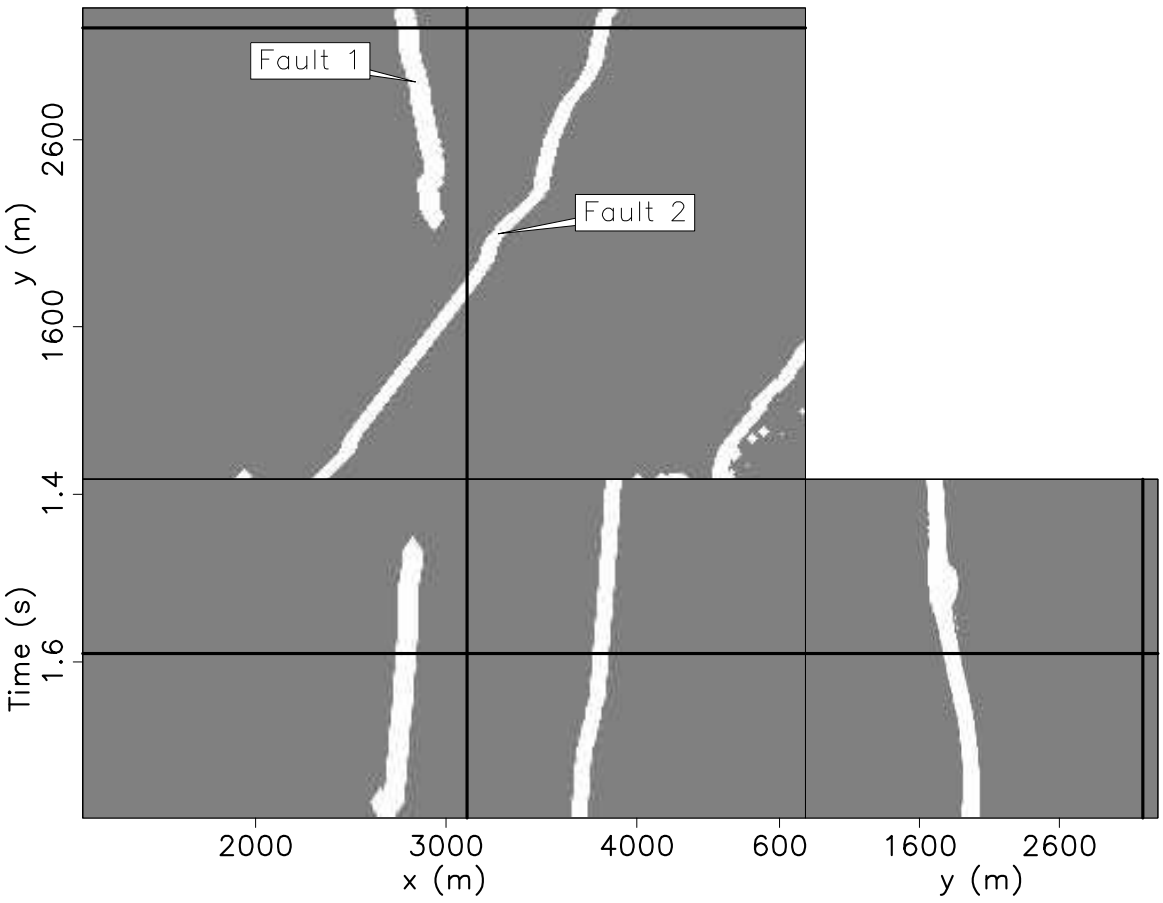
Fault 1
Fault 2
y (m)
2600
1600
Time (s)
1.4
1.6
2000
3000
x (m)
4000
600
1600
2600
y (m)

Figure 11.

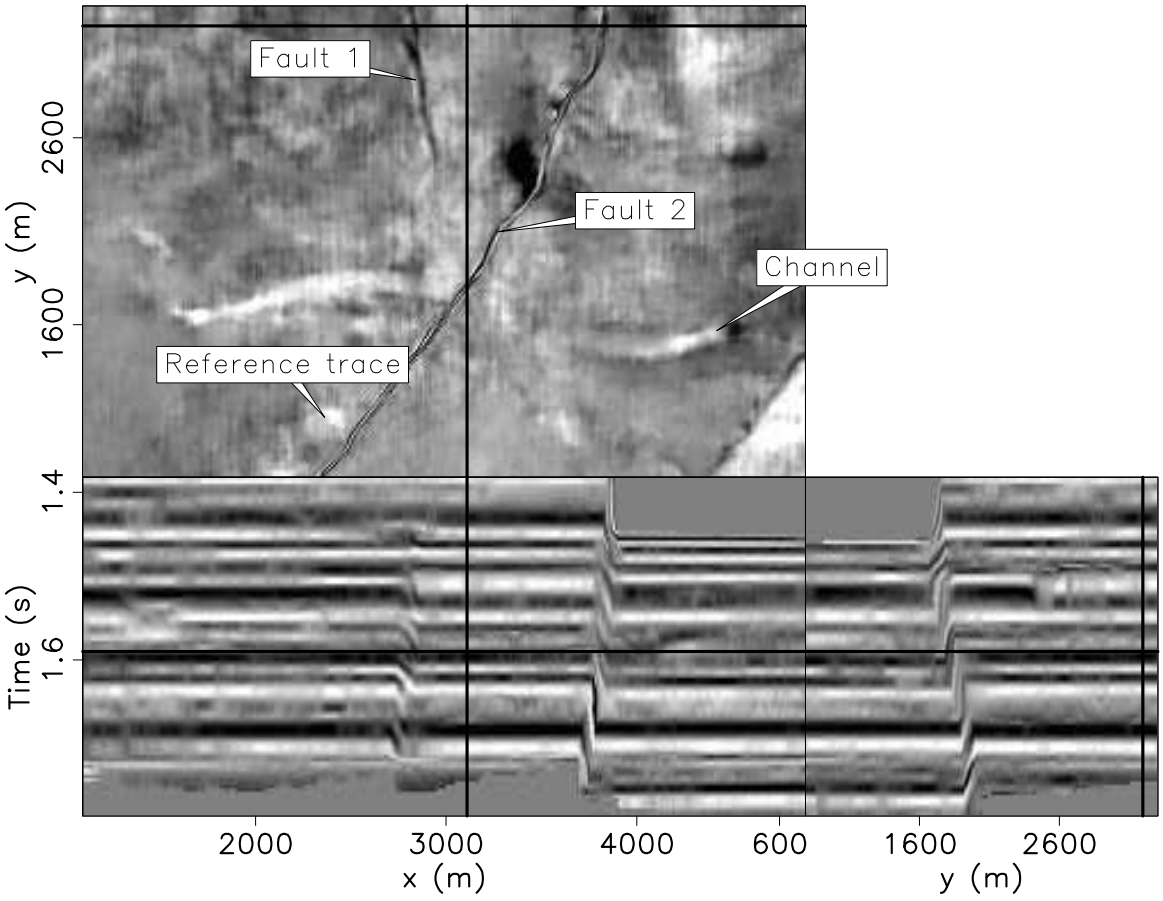
Fault 1
Fault 2
Channel
Reference trace
y (m)
2600
1600
Time (s)
1.4
1.6
2000
3000
x (m)
4000
600
1600
2600
y (m)

Figure 12.

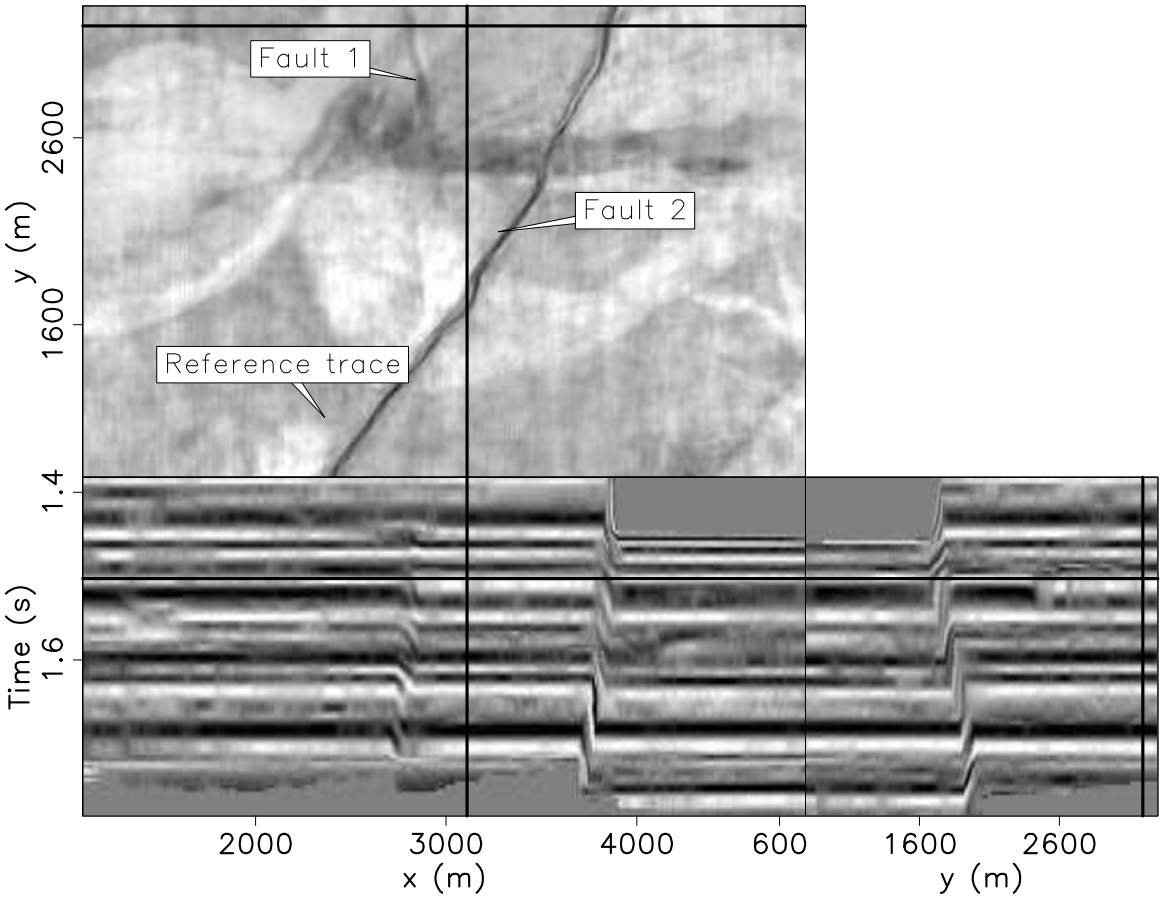
Fault 1
Fault 2
Reference trace
y (m)
2600
1600
Time (s)
1.4
1.6
2000
3000
x (m)
4000
600
1600
2600
y (m)

Figure 13.

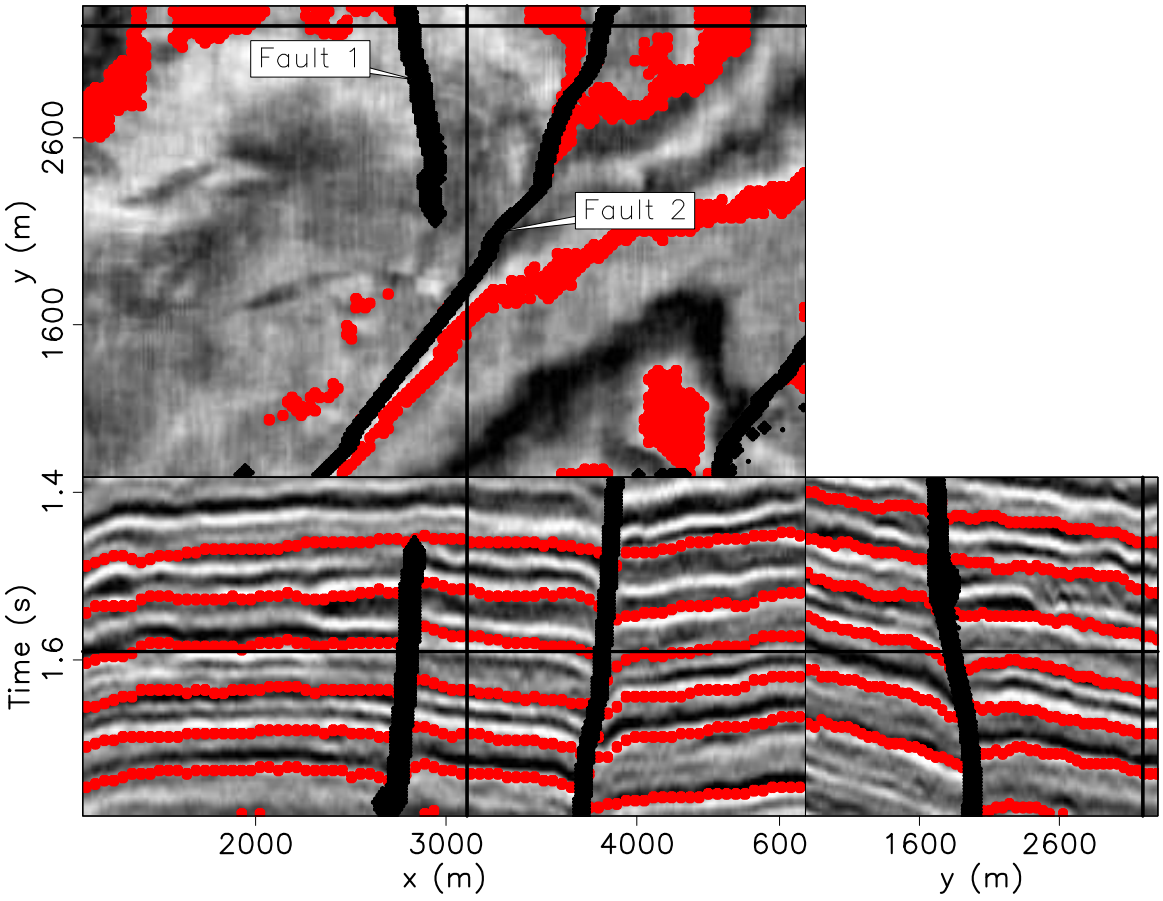
Fault 1
Fault 2
y (m)
2600
1600
1.4
Time (s)
1.6
2000
3000
x (m)
4000
600
1600
2600
y (m)

Figure 14.

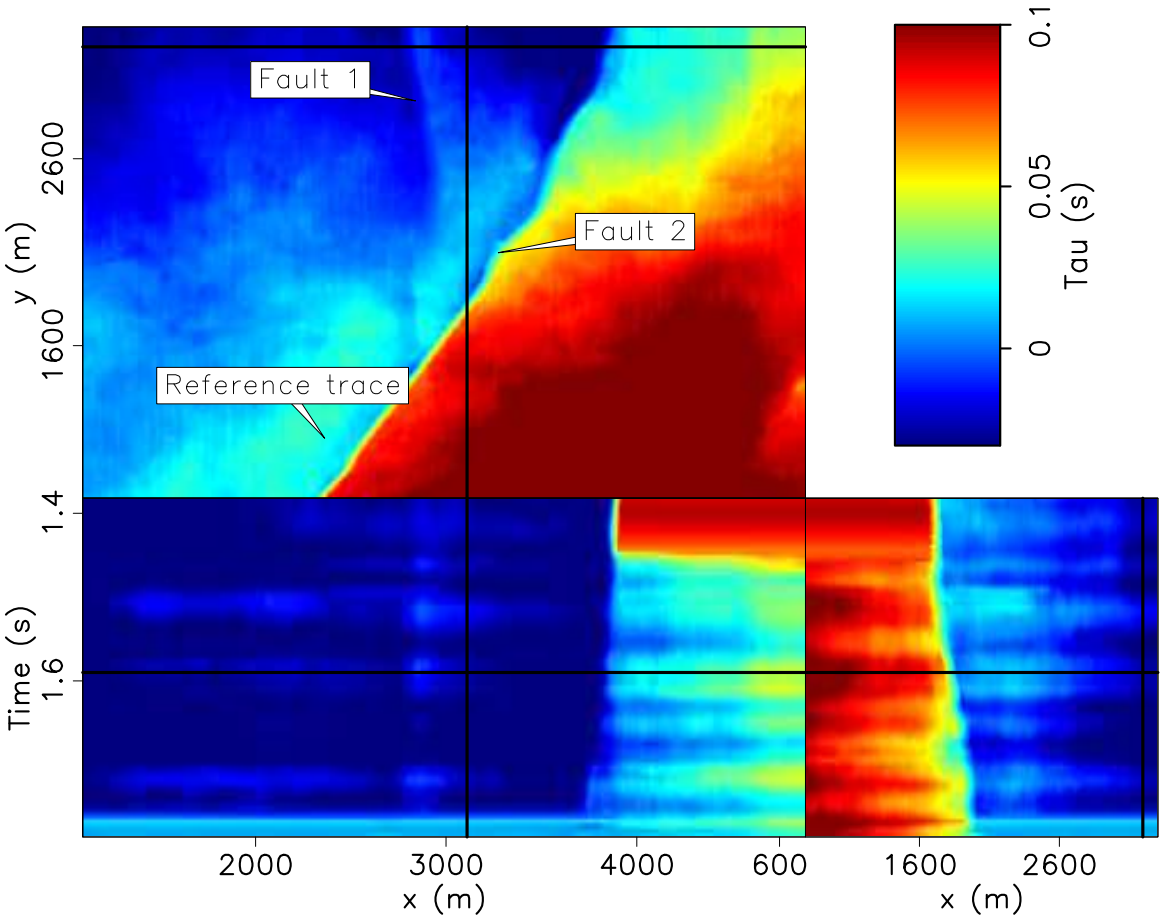
Fault 1
Fault 2
Reference trace
y (m)
2600
1600
Time (s)
1.4
1.6
0.1
0.05
0
Tau (s)
2000
3000
4000
600
1600
2600
x (m)
x (m)

Figure 15.

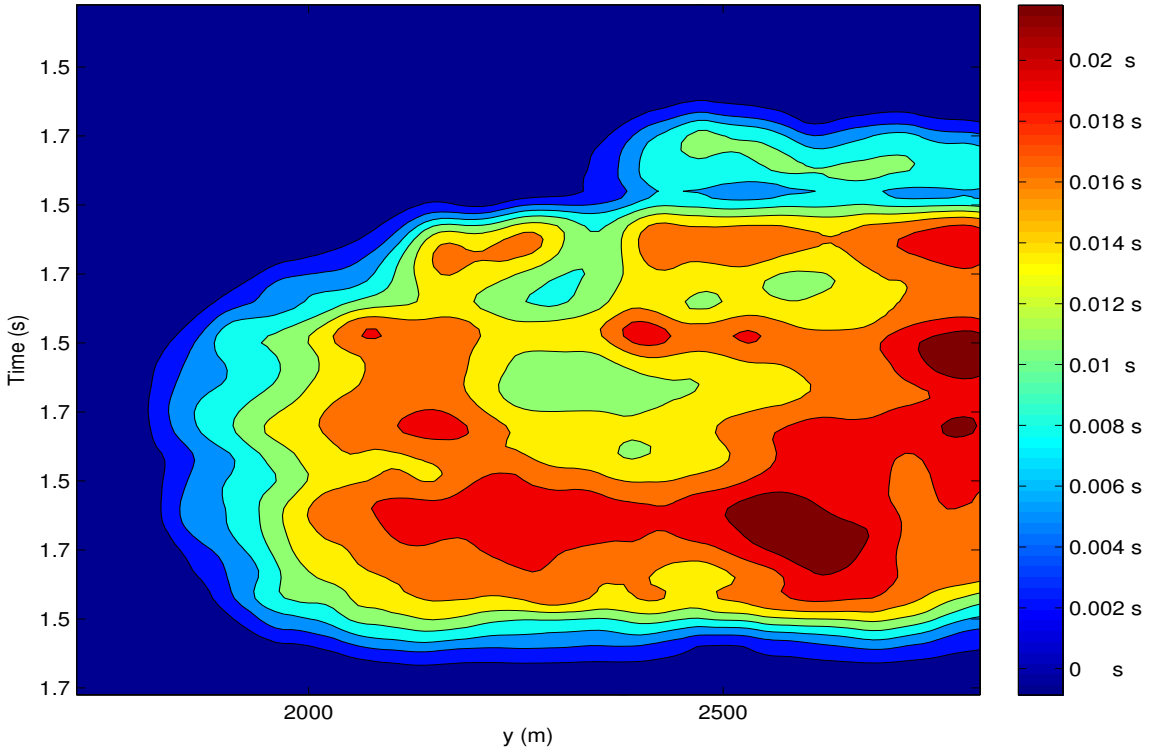
Time (s)
1.5
1.7
1.5
1.7
1.5
1.7
1.5
1.7
1.5
1.7
2000
2500
y (m)
0.02 s
0.018 s
0.016 s
0.014 s
0.012 s
0.01 s
0.008 s
0.006 s
0.004 s
0.002 s
0 s

Figure 16.

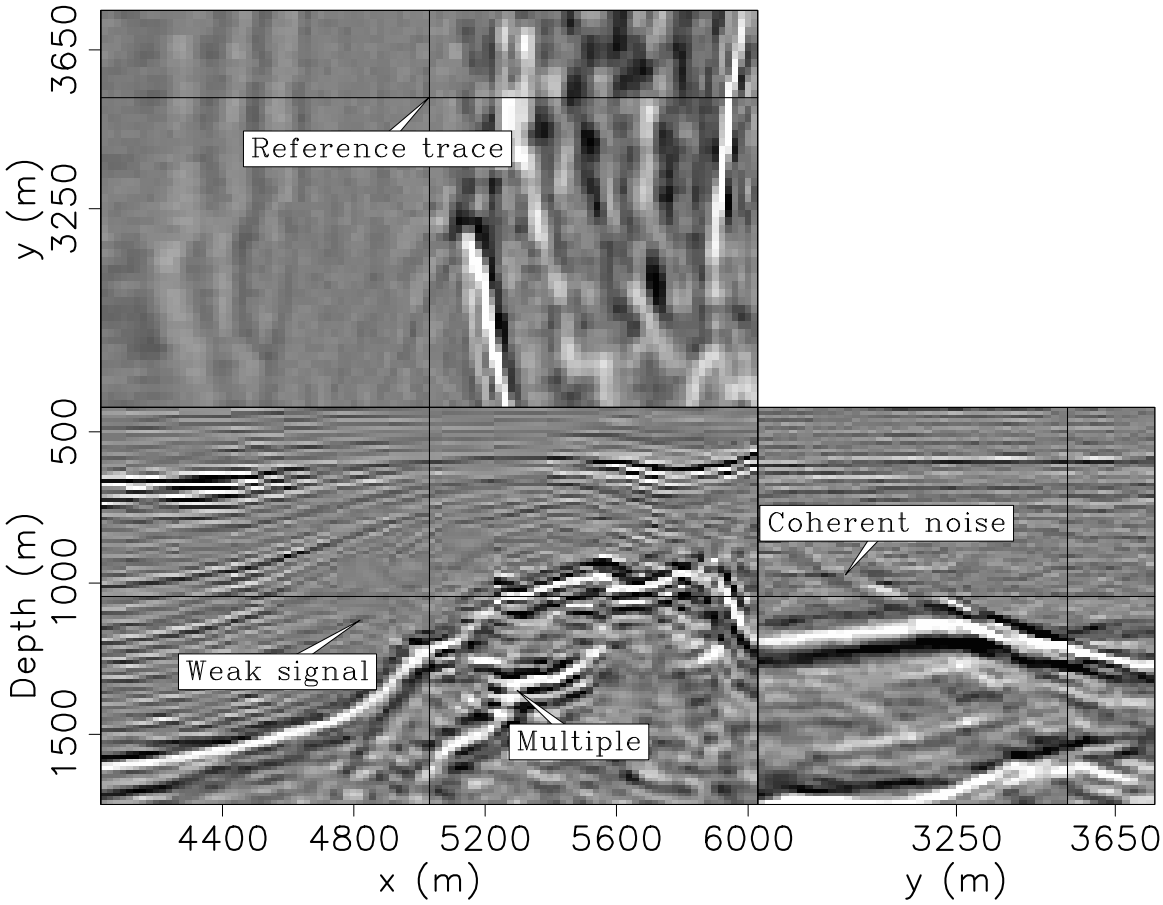
Reference trace
Coherent noise
Weak signal
Multiple
y (m)
3650
3250
Depth (m)
500
1000
1500
4400
4800
5200
5600
6000
x (m)
3250
3650
y (m)

Figure 17.

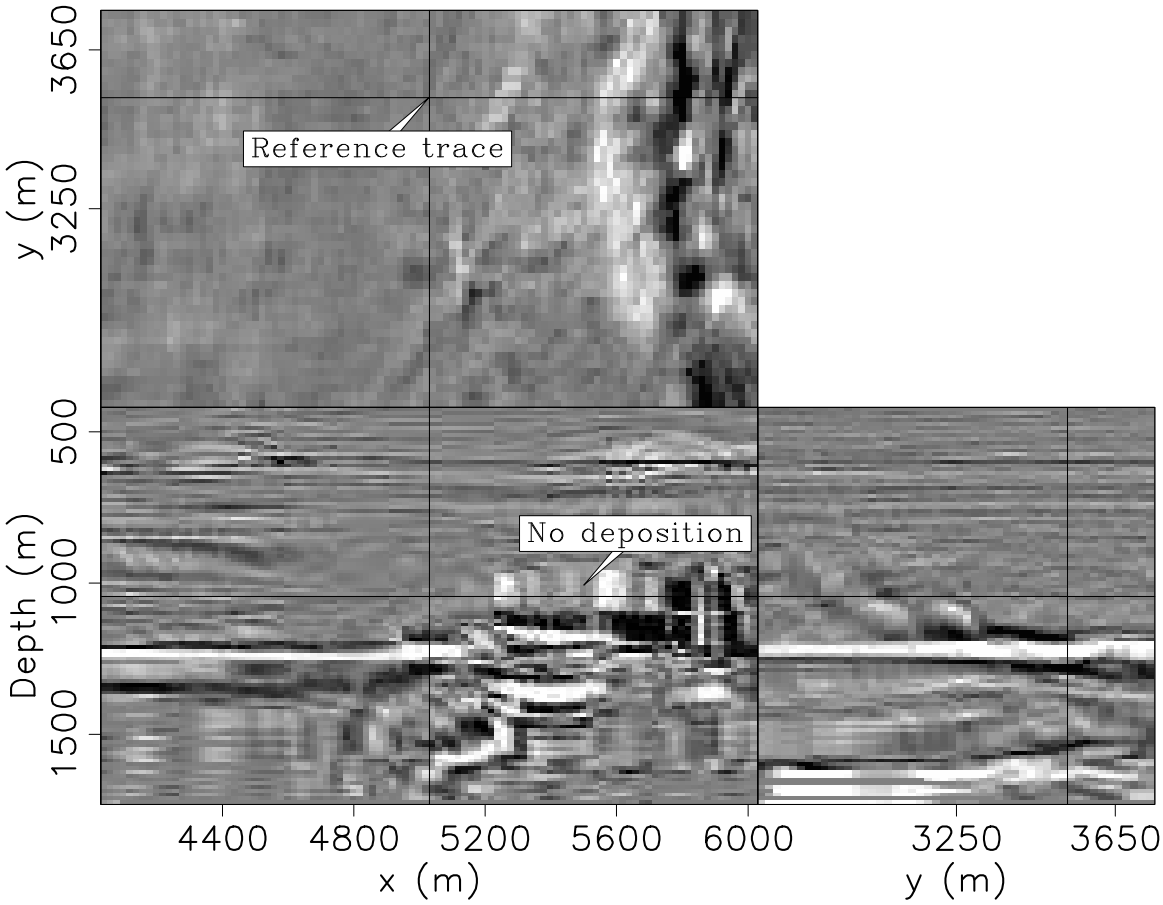
Reference trace
No deposition
y (m)
3650
3250
Depth (m)
500
1000
1500
4400
4800
5200
5600
6000
x (m)
3250
3650
y (m)

Figure 18.

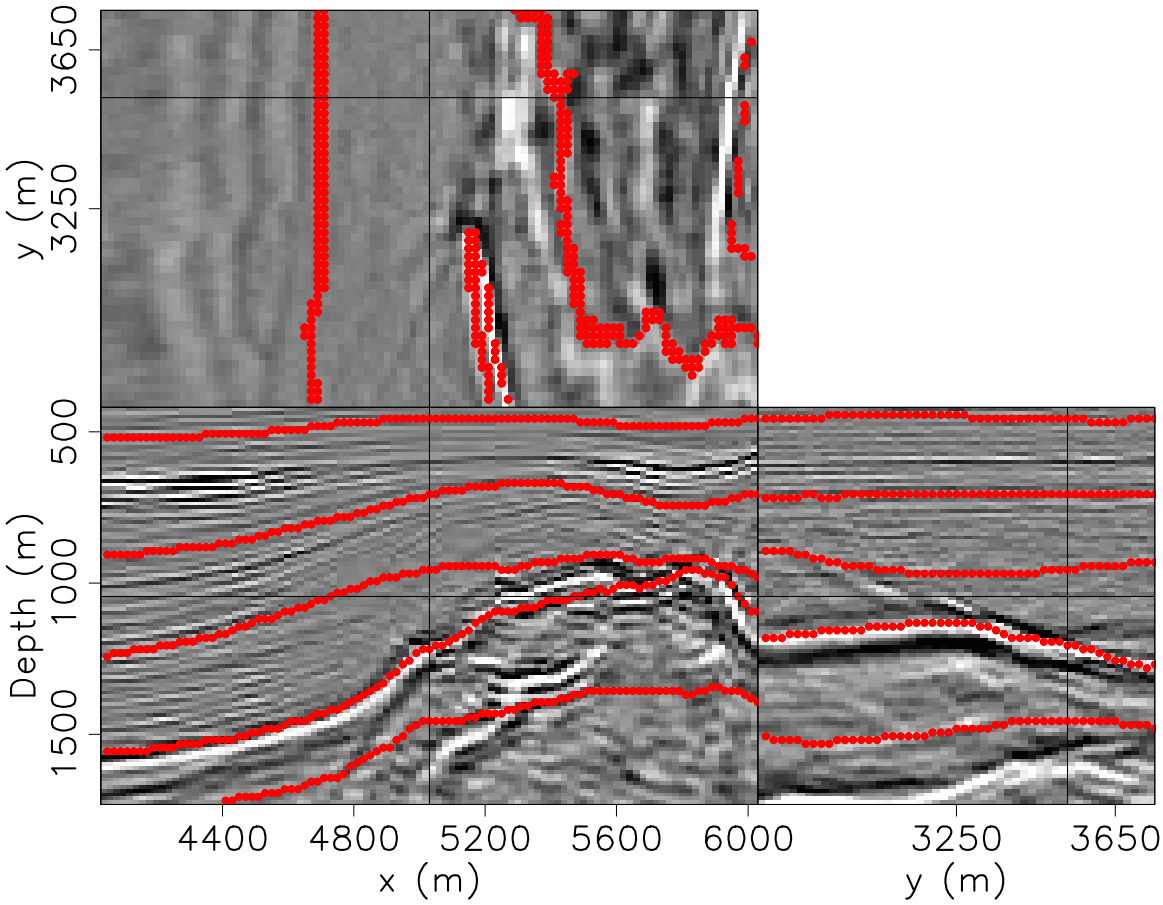
y (m)
3650
3250
500
Depth (m)
1000
1500
4400
4800
5200
5600
6000
x (m)
3250
3650
y (m)

Figure 19.

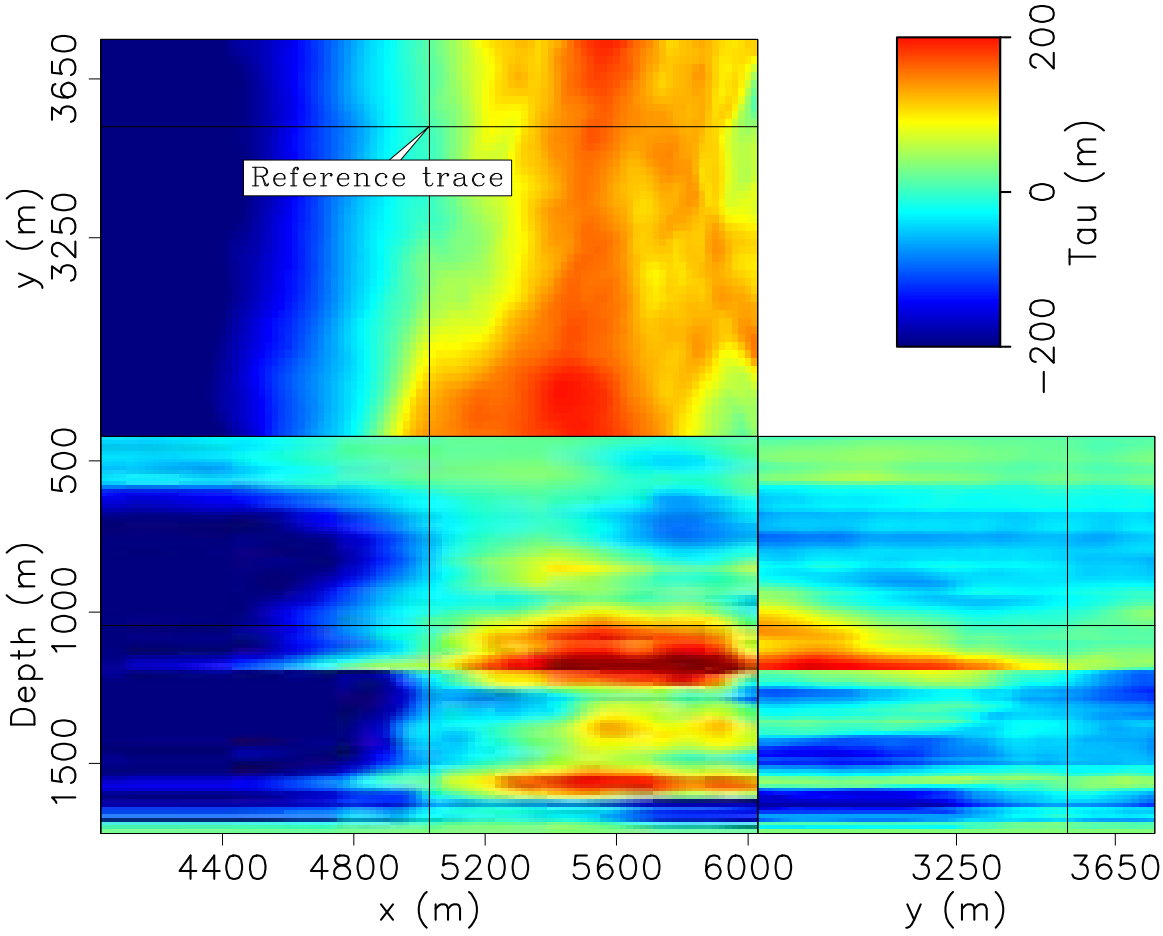
Reference trace
y (m)
3650
3250
Depth (m)
500
1000
1500
4400
4800
5200
5600
6000
x (m)
3250
3650
y (m)
200
0
−200
Tau (m)

Figure 20.

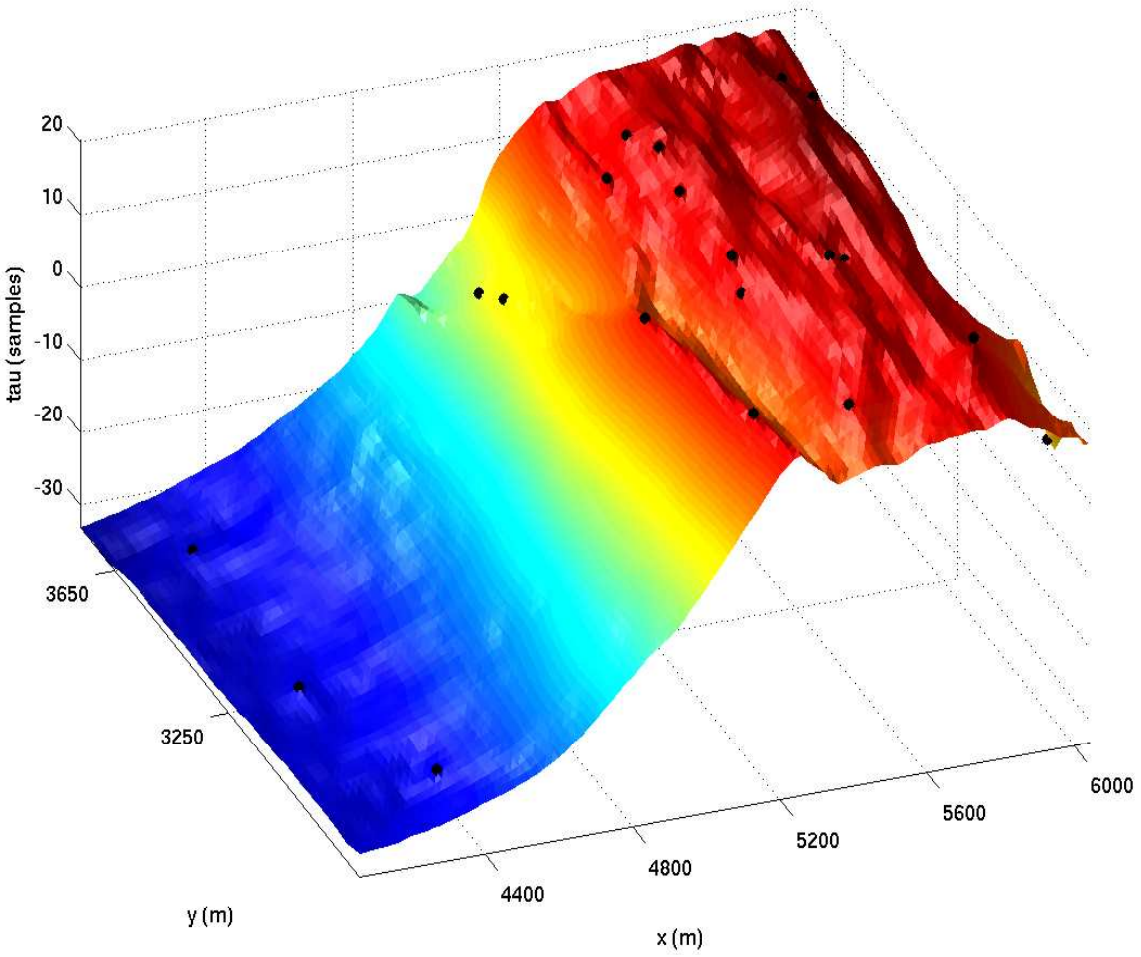
20
10
0
-10
-20
-30
tau (samples)
3650
3250
y (m)
4400
4800
5200
5600
6000
x (m)

Figure 21.

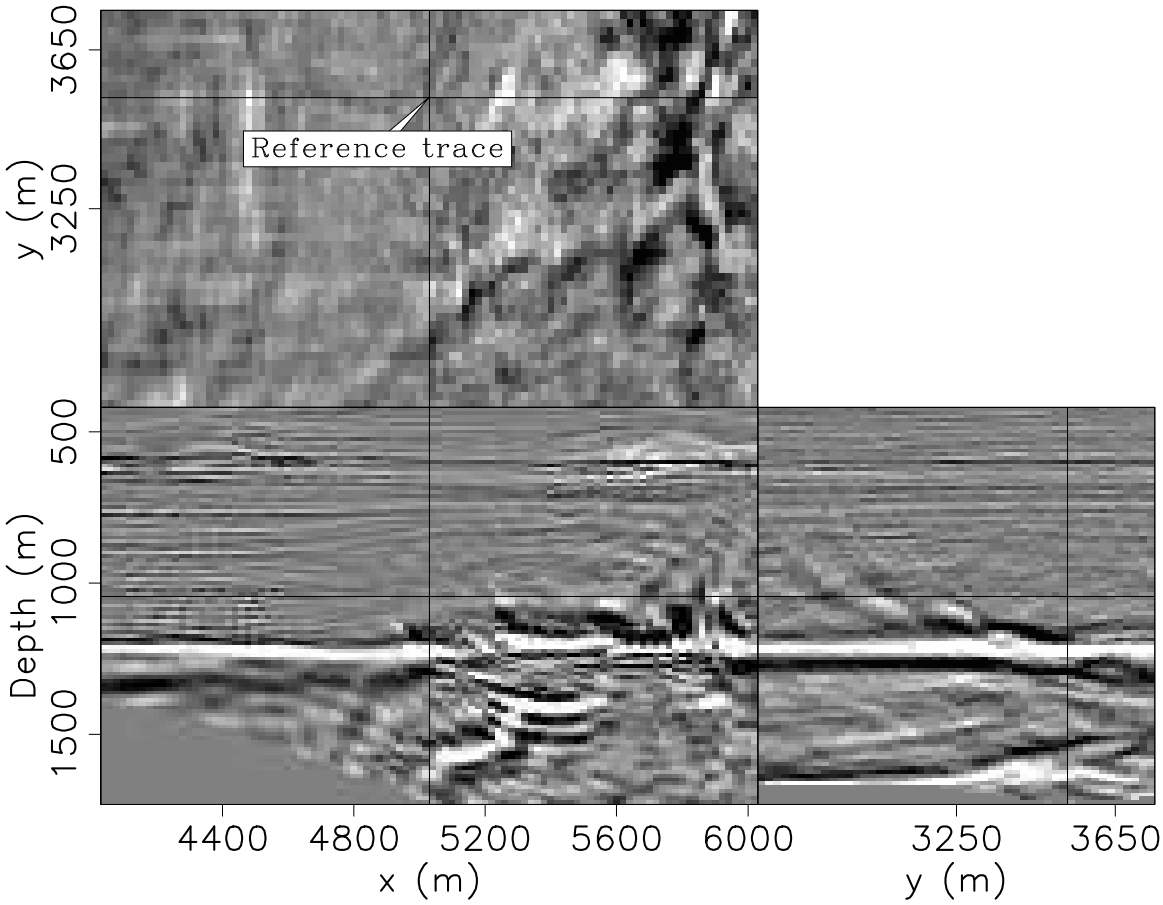
Reference trace
y (m)
3650
3250
Depth (m)
500
1000
1500
4400
4800
5200
5600
6000
x (m)
3250
3650
y (m)

Figure 22.

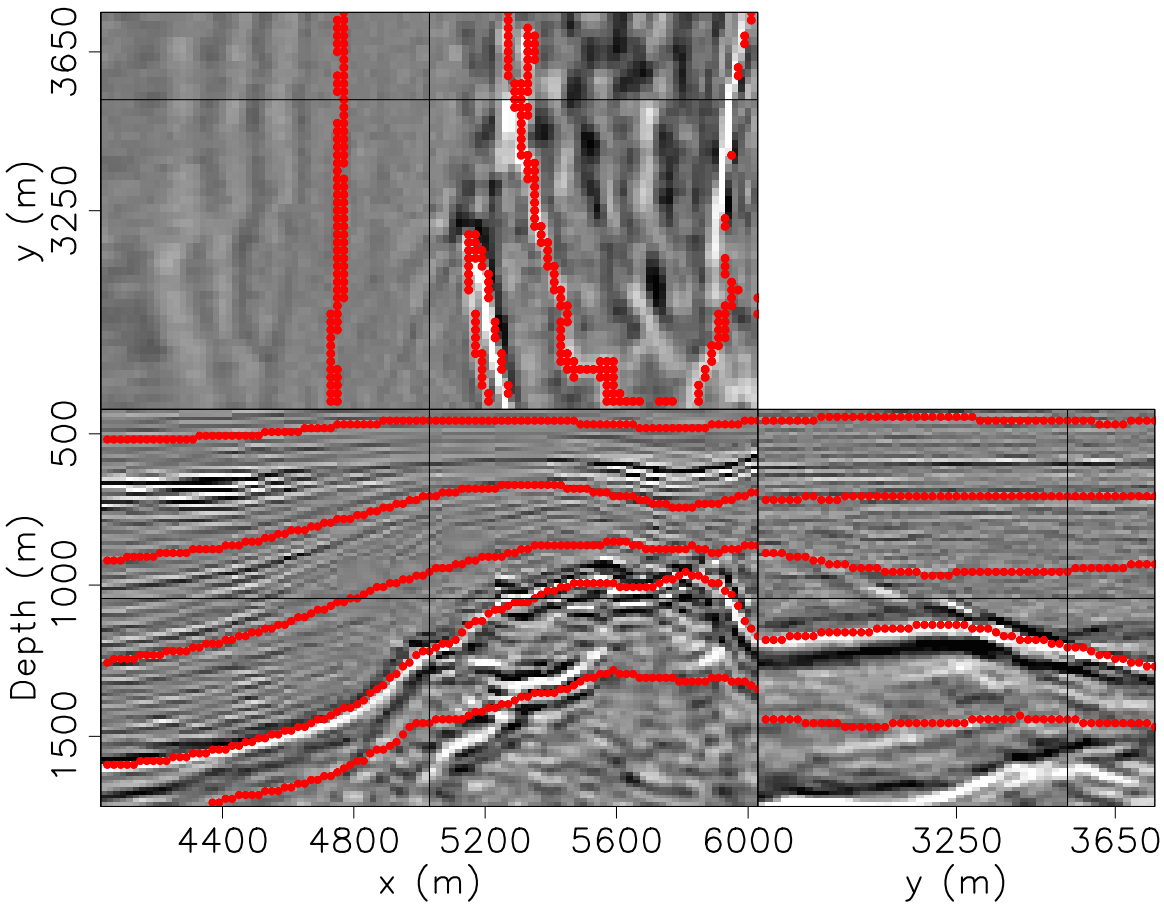
y (m)
3650
3250
Depth (m)
500
1000
1500
4400
4800
5200
5600
6000
x (m)
3250
3650
y (m)

Figure 23.